Submesoscale Dynamics near a Seamount. Part II: The Partition of Energy between Internal Waves and Geostrophy

ERIC KUNZE

School of Oceanography, University of Washington, Seattle, Washington

ABSTRACT

Using velocity and temperature profile surveys collected beside a seamount, the dependence of the energy ratio PE/KE on the aspect ratio $(Nk_H/fk_z)^2$ is compared with theoretical relations for linear internal waves and geostrophy. The kinetic and potential energies are partitioned between these two types of motion. The vertical wavelengths of 50–400 m and horizontal wavelengths of 1–20 km spanned by the measurements have traditionally been associated with internal waves. Most of the energy is in the largest vertical and horizontal scales. This larger-scale energy is split between internal waves and geostrophy in one survey and is all geostrophic in the other. Both internal waves and geostrophy contribute to smaller scales.

1. Introduction

Ocean fluctuations with vertical wavelengths less than a few hundred meters and horizontal wavelengths less than a few kilometers are usually interpreted as internal gravity waves (e.g., Garrett and Munk 1979). However, Holloway (1983) and Müller (1984) have questioned this view, pointing out that fluctuations that carry Ertel vorticity anomalies (e.g., geostrophic) can coexist on these same scales.

The challenge for observationalists is to find methods to distinguish between these two kinds of motion in the sea. Internal waves have intrinsic frequencies $f < \omega < N$, where f is the Coriolis frequency and N the buoyancy frequency, while Ertel vorticity–carrying fluctuations are subinertial ($\omega \ll f$). This allows identification of the dynamics of large-scale fluctuations (which are little affected by advective nonlinearity) with moored time series measurements. However, smaller scales become increasingly Doppler smeared so that frequency cannot reliably be used to distinguish finescale internal waves from Ertel vorticity–carrying motions. A significant breakthrough was made by Sherman and Pinkel (1991), who transformed CTD profile time series of finescale strain ξ_z into isopycnal-following coordinates, thus removing the effects of vertical Doppler advection. In this "semi-Lagrangian" frame, most of the finescale strain fluctuations appeared to be attributable to near-inertial internal waves. Anderson and Pinkel (1993) reached the same conclusion for finescale shear.

An unambiguous distinguishing property is the Ertel potential vorticity anomaly $\delta\Pi = (f + \nabla \times \mathbf{V}) \cdot \nabla b - f\bar{N}^2$ (Riley et al. 1981; Müller 1984), where $b = -g\delta\rho/\rho_0$ is the buoyancy and $\bar{N}^2$ the background buoyancy frequency squared. Internal waves do not have Ertel vorticity anomalies because $\delta\Pi$ can only be modified by irreversible processes (Ertel 1942; Pedlosky 1979; Haynes and McIntyre 1987). For example, Lelong and Riley (1991) have shown that weak triad wave–wave and wave–vortex interactions do not modify Ertel vorticity, and vortices appear in numerical simulations of forced "internal waves" only if the forcing directly induces Ertel vorticity anomalies (Herring and Metais 1989).

Measuring finescale Ertel vorticity in the ocean is a daunting undertaking. Müller et al. (1988) attempted to estimate the linear Ertel vorticity perturbation $f\bar{N}^2(\xi_z + \zeta/f)$, where ζ is the relative vorticity, using the Internal Wave Experiment (IWEX) trimooring data (Müller et al. 1978). Unfortunately, a three-point array cannot distinguish relative vorticity and horizontal divergence if the dominant signal is from scales at or smaller than the array size as is the case in the ocean (Lien and Müller 1992b). Kunze and Sanford (1993) describe measurements of submesoscale Ertel vorticity anomalies on vertical wavelengths $\lambda_z = 50$–400 m and horizontal wavelengths $\lambda_H \approx 7$–15 km beside Ampere Seamount. They find these motions to be in geostrophic balance with only the linear Ertel vorticity terms contributing significantly.

Lien and Müller (1992a) formulated complete sets of consistency relations for linear internal waves and geostrophy. In this paper, we make use of one of these. We examine the dependence of the ratio of available potential to horizontal kinetic energy $R_E = \text{PE}/\text{KE}$ (or

Corresponding author address: Dr. Eric Kunze, School of Oceanography, University of Washington, Seattle, WA 98195.

energy Burger number) on normalized aspect ratio R_L = $(N\lambda_z/f\lambda_H)^2$ (or length scale Burger number) using the velocity and temperature profile surveys of Kunze and Sanford (1993). The results are compared to the expected relationships for internal waves and geostrophy (to be described in section 3).

2. Data

The measurements consist of two synoptic cross-shaped velocity and temperature profile (XCP) surveys, an XBT box survey, and six CTD casts (Fig. 1). The XCP surveys were collected a few kilometers east of Ampere Seamount in the eastern North Atlantic during September 1988 (Kennelly et al. 1989). Survey 1 was made on the northwest flank of the seamount while survey 2 was a few kilometers to the southeast. They contained 28 profiles each, were ~7 km in diameter, and had 0.3–1.0-km station spacing. The CTD casts were also collected east of Ampere Bank (Fig. 1). The XBT survey was 60 km on a side and centered on the seamount; it encompasses the domain shown in Fig. 1.

The expendable current profiler (XCP) measures horizontal velocity (relative to an unknown but depth-independent constant) and temperature from the surface to depth ~1600 m (Sanford et al. 1982). As we will be confining our attention to vertical wavelengths less than 400 m, the unknown barotropic velocity is of no concern. Velocity is measured electromagnetically. It has an rms noise level of 0.4 cm s^{-1} or a kinetic energy error of 0.1 cm^2 s^{-2} that limits vertical resolution to 3 m in the ocean pycnocline. Temperature is measured with an XBT thermistor to ±0.06°C, which corresponds to rms buoyancy errors of 6 × 10^{-5} m s^{-2} (given $\partial b/\partial T \simeq 10^{-3}$ m s^{-2} °C^{-1}; Kunze and Sanford 1993), an rms vertical displacement error of ~5 m, and potential energy noise of 1.5 cm^2 s^{-2} (given N_0 $\simeq$ 3.5 × 10^{-3} s^{-1}). The temperature measurement is the largest source of error in computing the energy, contributing an order of magnitude greater error than the velocity measurement. This restricts estimation of the available potential energy to vertical wavelengths larger than 20 m.

Expendible current profilers (XCPs) can be deployed from a ship under way, making them suitable for rapid near-synoptic surveying of submesoscale horizontal structure in the ocean. Each XCP survey was completed in under 3 h to minimize temporal aliasing of the spatial structure. Despite these precautions, the horizontal structure for vertical wavelengths smaller than 50 m was temporally contaminated (Kunze and Sanford 1993) so we restrict our attention to larger wavelengths.

The XCP surveys provide $u(x, y, z)$, $v(x, y, z)$, and $T(x, y, z)$. To obtain buoyancy anomalies b = $-g\delta\rho/\rho_0$ = $-N^2\xi$, we use the CTD profiles to convert temperature T to total buoyancy $\bar{B}(z) + b$ (density). This confines our attention to depths of 150–600 m
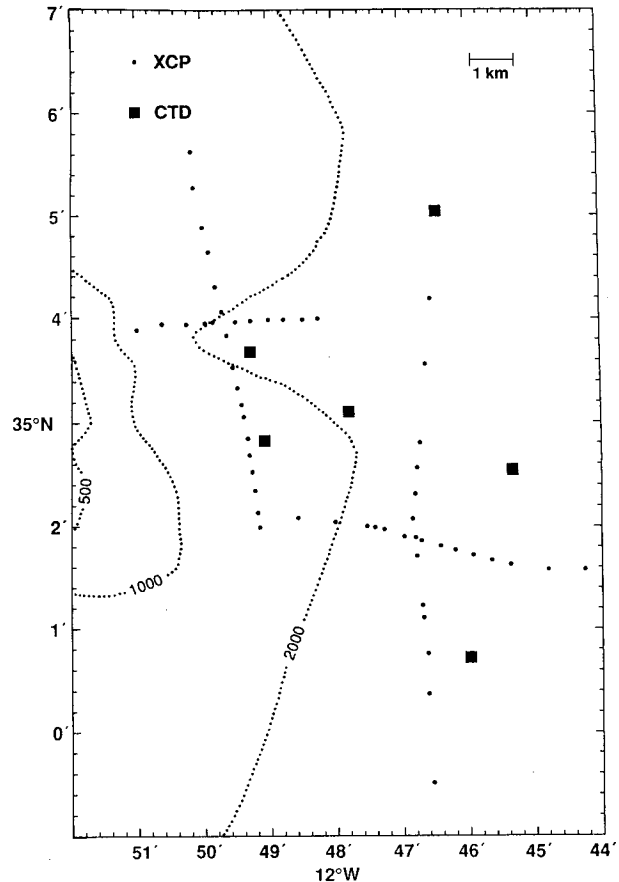

FIG. 1. Sampling off the eastern flank of Ampere Bank. Bathymetry is in meters. Two cross-shaped velocity and temperature profile (XCP) surveys were made, each in under 3 hours. Six CTD casts were taken to determine the T–σ_θ relation.

where the T–σ_θ relation is tight (Kunze and Sanford 1993). In this depth range, $\bar{N}(z)$ = 3.3–3.7 × 10^{-3} s^{-1}. The background buoyancy profile $\bar{B}(z)$ as deduced from the average of the larger scale XBT survey was subtracted from the total to obtain buoyancy anomalies $b(x, y, z)$. More detailed accounts of the measurements at Ampere Seamount and the data processing can be found in Kennelly et al. (1989) and Kunze and Sanford (1993).

3. Theoretical background: Energy ratio PE/KE versus aspect ratio $(Nk_H/fk_z)^2$

With horizontal velocities u and v, we can compute horizontal kinetic energy KE = $(u^2 + v^2)/2$ and, from buoyancy anomalies b, deduce the available potential energy PE = $b^2/(2\bar{N}^2)$ ≡ $\bar{N}^2\xi^2/2$. Kunze et al. (1990), D'Asaro and Morehead (1991), and Lien and Müller (1992a) have shown that the relationship between the energy ratio (or energy Burger number) R_E = PE/KE and the normalized aspect ratio (or length scale Burger number) R_L = $(Nk_H/fk_z)^2$ can be used to distinguish

linear internal gravity waves from baroclinic geo-
strophic motion (Fig. 2).

For linear internal gravity waves, the energy ratio
depends on intrinsic frequency ω as

$$R_{E_{IW}} = \frac{PE}{KE} = \frac{N^2(\omega^2 - f^2)}{(N^2 - \omega^2)(\omega^2 + f^2)} \qquad (1)$$

(Fofonoff 1969; Müller and Siedler 1976). Applying
the linear internal wave dispersion relation

$$\omega^2 = \frac{f^2 k_z^2 + N^2 k_H^2}{k_z^2 + k_H^2} = f^2 \frac{1 + R_L}{1 + (f^2/N^2)R_L}, \qquad (2)$$

the internal wave energy ratio (1) can be expressed as
a function of the normalized aspect ratio

$$R_{E_{IW}} = \frac{PE}{KE} \simeq \frac{R_L(1 + (f^2/N^2)R_L)}{(R_L + 2)} \qquad (3)$$

for $N^2 \gg f^2$. This is described by the thick dotted curve
in Fig. 2. The sloping part of the curve to the left of
$(Nk_H/fk_z)^2 = 3$ corresponds to near-inertial waves (ω
$\simeq f$), the slope to the right of $(Nk_H/fk_z)^2 = 300$ to
near-buoyancy frequency waves ($\omega \simeq N$), and the flat
segment with PE/KE $\simeq 1$ in between to continuum
internal waves ($f \ll \omega \ll N$). Relation (3) holds in the
presence of advective nonlinearity and is therefore in-
sensitive to Doppler smearing.

For Ertel vorticity–carrying motions satisfying the
linear momentum equations (geostrophic), the ther-
mal-wind relation implies

$$R_{E_g} = \frac{PE}{KE} = \frac{1}{R_L} = \left(\frac{fk_z}{Nk_H}\right)^2, \qquad (4)$$

which is described by the thick-dashed diagonal in Fig.
2. Therefore, the low-aspect-ratio geostrophic motions
on basin scales (low k_H) have much more potential
than kinetic energy.

For low Froude number ($V_z/N \ll 1$) high Rossby
number Ertel vorticity–carrying flow, horizontal (iso-
pycnal) motions are approximately described by

$$uu_x + vu_y - fv = -p_x,$$
$$uv_x + vv_y + fu = -p_y, \qquad (5)$$

where the "kinematic" pressure $p = P/\rho_0$ and the x
and y derivatives lie along isopycnals—plus the hydro-
static balance and isopycnal nondivergence (Riley et
al. 1981; Lilly 1983; Müller 1984). The isopycnal shear
can be decomposed into isopycnal divergence: $\nabla = u_x$
$+ v_y$; relative vorticity: $\zeta = v_x - u_y$; and two conflu-
ences: $S_1 = u_x - v_y$ and $S_2 = v_x + u_y$. For Ertel vorticity–
carrying motions, the isopycnal divergence ∇ must be
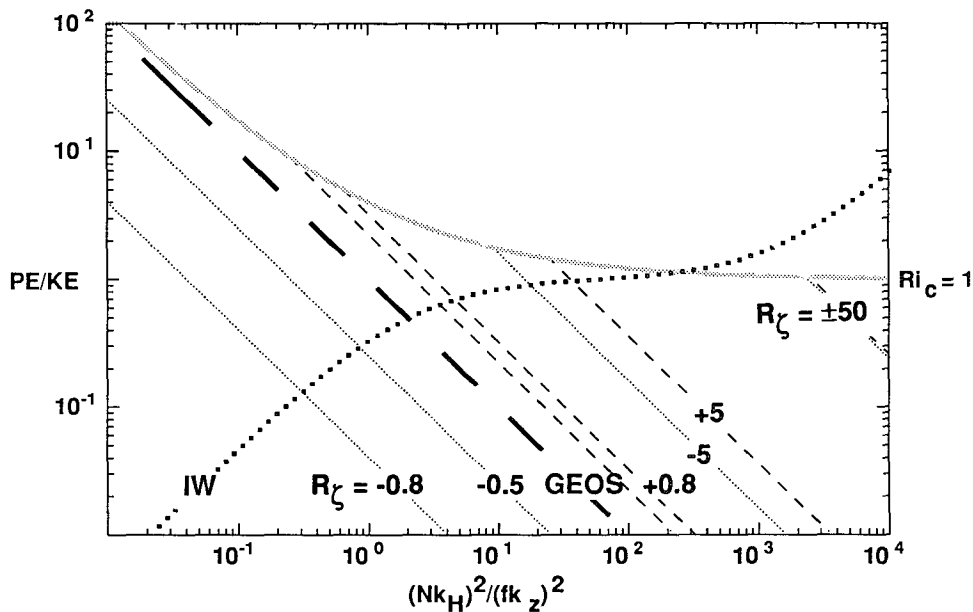small (by analogy to geostrophic flow) to prevent rapid

FIG. 2. A dynamic diagram describing the dependence of energy ratio R_E = PE/KE (energy Burger
number) on scaled aspect ratio $R_L = (Nk_H/fk_z)^2$ (length scale Burger number) after D'Asaro and Morehead
(1991), where PE is the available potential energy and KE the horizontal kinetic energy. The $\sim$ curve is the
relation for linear internal waves with $N/f = 40$ (3). The thick dashed diagonal corresponds to geostrophy
(4). The thin diagonals correspond to nonzero vorticity Rossby number $R_\zeta = \zeta/f$ Ertel vorticity–carrying
motions of negative (dotted) and positive (dashed) relative vorticity (9). Nonzero Rossby number Ertel
vorticity–carrying fluctuations in the domain above the $Ri_c = 1$ curve have vertical shears exceeding the
buoyancy frequency N.

modification of the density field. Likewise, the horizontal pressure gradients can be reexpressed as $f\Sigma_1 = -2p_{xy}, f\Sigma_2 = p_{xx} - p_{yy}$ and $fZ = p_{xx} + p_{yy}$. Therefore, the velocities and pressure gradients can be Taylor expanded as

$$u = u_o + u_x x + u_y y + \cdots$$
$$= u_o + (S_1/2)x + ((S_2 - \zeta)/2)y + \cdots$$
$$v = v_o + v_x x + v_y y + \cdots$$
$$= v_o + ((S_2 + \zeta)/2)x - (S_1/2)y + \cdots$$
$$p_x = X + p_{xx}x + p_{xy}y + \cdots$$
$$= X + (f(\Sigma_2 + Z)/2)x - (f\Sigma_1/2)y + \cdots$$
$$p_y = Y + p_{xy}x + p_{yy}y + \cdots$$
$$= Y - (f\Sigma_1/2)x - (f(\Sigma_2 - Z)/2)y + \cdots. \quad (6)$$

Substituting (6) into (5) and gathering terms proportional to x and y, one can show that

$$S_1 = \Sigma_1$$
$$S_2 = \Sigma_2$$
$$\zeta^2 + 2f\zeta = \Sigma^2 + 2fZ, \quad (7)$$

where $\Sigma^2 = \Sigma_1^2 + \Sigma_2^2 = S_1^2 + S_2^2 = S^2$ (Kunze et al. 1990). This demonstrates that the confluences $S_{1,2}$ obey the geostrophic momentum equations regardless of their magnitude and that only the relative vorticity ζ contributes to momentum nonlinearity as the Rossby number increases. In terms of these parameters, the energy ratio can be expressed as

$$\frac{PE}{KE} = \frac{1}{R_L}\left(\frac{\Sigma^2 + Z^2}{S^2 + \zeta^2}\right) = \frac{1}{R_L}\left(\frac{S^2 + Z^2}{S^2 + \zeta^2}\right) \quad (8)$$

so that a pure confluence field satisfies the geostrophic relation (4) and a pure vorticity field (e.g., solid-body rotation) satisfies

$$\boxed{R_{E_\zeta} = \frac{PE}{KE} = \frac{(1 + R_\zeta/2)^2}{R_L}} \quad (9)$$

For nonlinear Ertel vorticity–carrying flow, where the vorticity Rossby number $R_\zeta = \zeta/f$ has the same sign as vorticity. For zero Rossby number, (9) reduces to the geostrophic relation (4). For Rossby numbers $O(1)$, the flow is in cyclogeostrophic balance with both relative and planetary vorticity important. For Rossby numbers $N/f > |\zeta|/f \gg 1$, earth's rotation can be neglected and the flow is cyclostrophic [low Froude number flow of this kind has been termed stratified turbulence by Riley et al. (1981) and Lilly (1983)]. For higher Rossby numbers, the shear is sufficient to overcome stratification and the flow will become fully three-dimensionally turbulent. Figure 2 displays relation (9) for various positive (thin dashed) and negative

(thin dot) vorticity Rossby numbers. These diagonals are parallel to the geostrophic relation (4). For $|\zeta|/f \gg 1$, they correspond to higher R_E (more relative potential energy) for a given R_L.

4. Analysis

To compare the observations with the Burger number dynamic diagram (Fig. 2), it is necessary to partition the horizontal kinetic and available potential energies in both vertical and horizontal wavenumber so that an appropriate aspect ratio $(Nk_H/fk_z)^2$ can be assigned. The profiles $u(z)$, $v(z)$, and $b(z)$ were first transformed into isothermal (isopycnal) coordinates. Fourier transforms were then applied to demeaned profiles of 128 points (400 m long) windowed with a 10% $\sin^2$ filter at both ends to obtain complex Fourier coefficients $\psi_r(k_z) + i\psi_i(k_z)$ as a function of vertical wavenumber. Because of temporal aliasing for vertical wavelengths less than 50 m (Kunze and Sanford 1993), valid analysis is limited to $\lambda_z = 50$–400 m, or the first nine Fourier modes of the transforms.

The next step is to partition the energy into horizontal wavenumbers. Since the two surveys are ~ 7 km in diameter with sample spacings of ~ 0.5 km, only horizontal wavelengths in the narrow band $\lambda_H = 1$–7 km can be resolved. This extends the analysis to smaller horizontal scales than could be treated by Kunze and Sanford (1993) because they fit over the smaller horizontal scales. Energy on scales larger than the surveys (k_H unresolved but bounded above by $2\pi/7$ km^{-1}) will be contained in survey averages and be referred to as *average* energy.

The average and residual energy spectra are compared to appropriately low- and high-pass horizontal-wavenumber filtered Garrett–Munk (GM) model spectra in Figs. 3 and 4. The variance-preserving spectra (right panels) reveal that the bulk of the energy is in the largest resolved vertical wavelength ($\lambda_z = 400$ m) for horizontal wavelengths greater than 7 km (Fig. 3). The average potential energy spectra are comparable to the kinetic energy spectra (unlike the dominance of kinetic over potential energy in the low-pass GM internal wave field).

For vertical wavelengths less than 200 m, the residual energy spectra (Fig. 4) exceed the average, consistent with the high-passed GM, indicating that most of the kinetic and potential energy in $\lambda_z < 200$ m is associated with horizontal wavelengths smaller than 7 km.

The residual fraction will contain energy in $\lambda_H = 1$–7 km, which will be referred to as resolved (̃), and in horizontal wavelengths smaller than 1 km (k_H unresolved but bounded below by $2\pi/1$ km^{-1}), which will be referred to as incoherent ('').

To separate the resolved and incoherent parts, we follow the methodology of D'Asaro and Morehead (1991). For each vertical wavenumber, the residual real and imaginary Fourier coefficients from individual profiles,
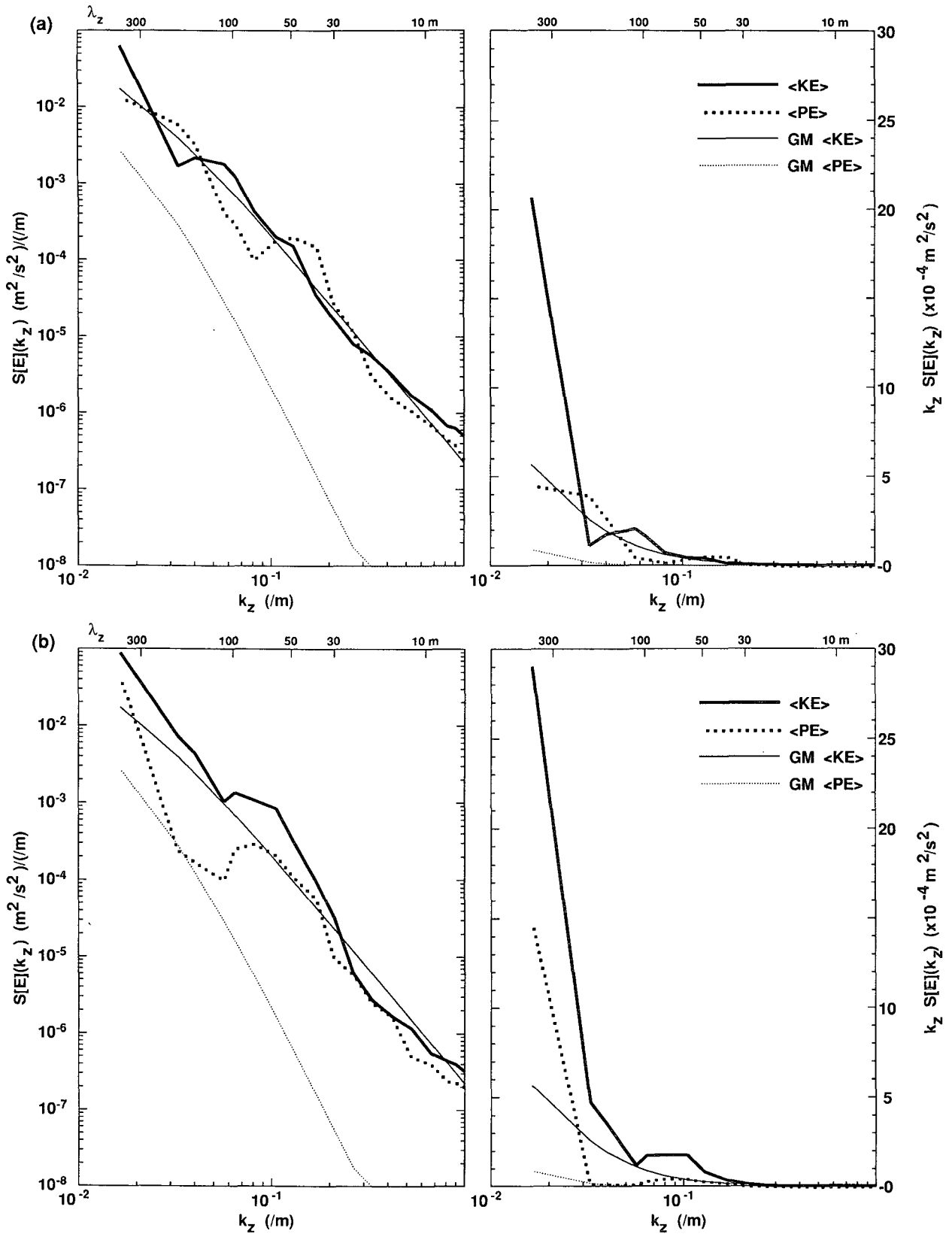
FIG. 3. Vertical wavenumber spectra for horizontal kinetic energy KE (thick solid) and available potential energy PE (thick dotted) in the survey averages are compared with the low-pass horizontal-wavenumber filtered GM model (thin solid and dotted) for surveys 1 (a) and 2 (b).
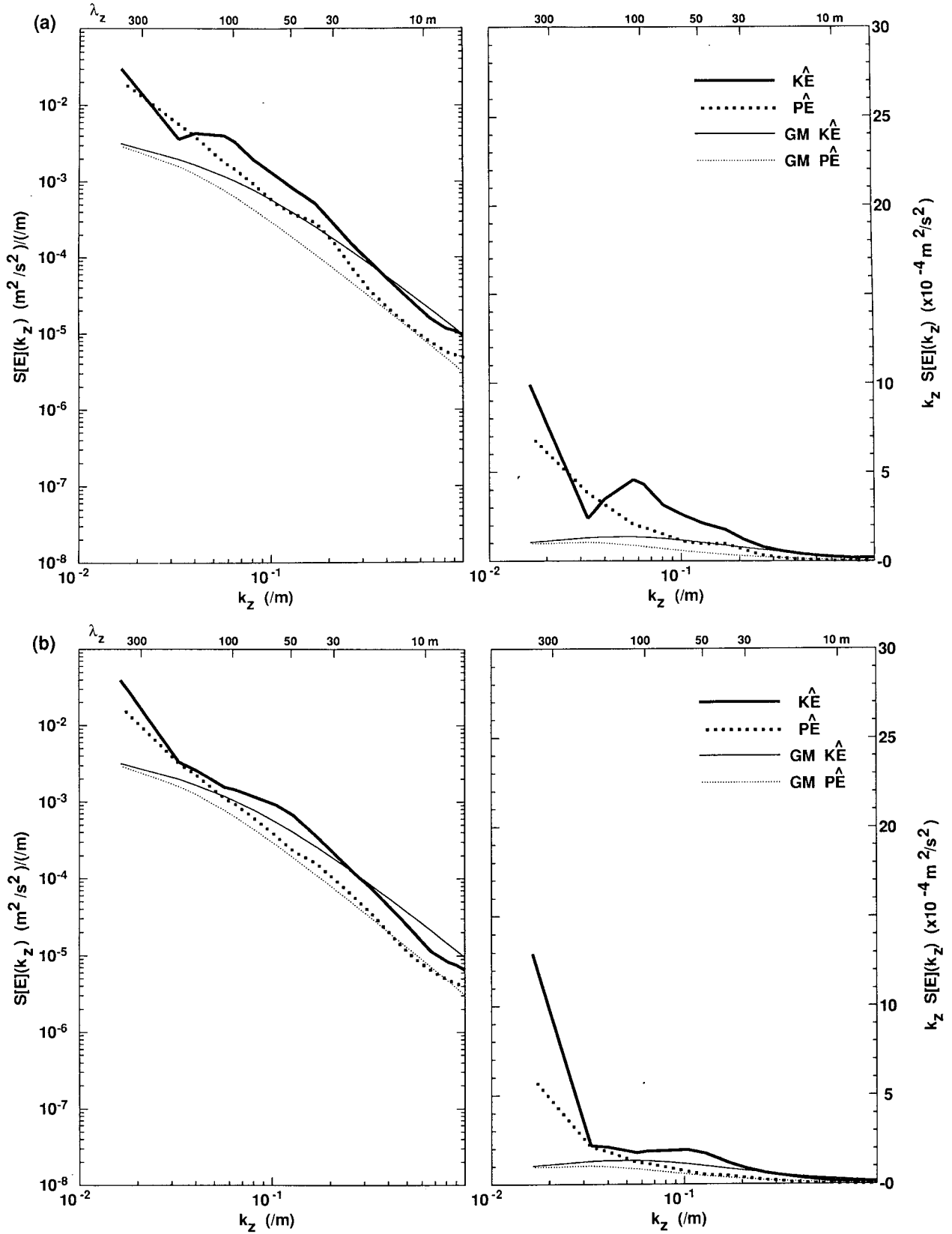
FIG. 4. Vertical wavenumber spectra for horizontal kinetic energy KE (thick solid) and available potential energy PE (thick dotted) in the survey residuals are compared with the high-pass horizontal-wavenumber filtered GM model (thin solid and dotted) for surveys 1 (a) and 2 (b).

$$\hat{\psi}_r(k_z) = \psi_r(k_z) - \langle \psi_r(k_z) \rangle;$$

$$\hat{\psi}_i(k_z) = \psi_i(k_z) - \langle \psi_i(k_z) \rangle, \qquad (10)$$

where $\langle \cdot \rangle$ denotes the survey average and $\hat{}$ the residuals are combined to form profile-pair correlations as a function of horizontal separation $\delta r = \sqrt{\delta x^2 + \delta y^2}$. For horizontally isotropic sampling, only the real part of the average correlation $\langle \mathrm{cor}_r \rangle$ is nonzero

$$\mathrm{cor}_{r_{mn}}[\hat{\psi}](k_z, \delta r) = \hat{\psi}_{r_m}\hat{\psi}_{r_n} + \hat{\psi}_{i_m}\hat{\psi}_{i_n}, \qquad (11)$$

where the m and n subscripts denote profiles m and n. Individual profile-pair correlations for $\lambda_z = 100$ m from survey 1 are displayed as gray dots in Fig. 5. The large scatter is typical of raw correlations in the ocean and signifies a broadband process. Only the radially smoothed (excluding $\delta r = 0$) correlation averages (dashed curves) are statistically meaningful. Average covariances at $\delta r = 0$ ($m = n$) are depicted by large black squares. The solid curves are fits to the raw correlations (excluding $\delta r = 0$) of a sum of approximately orthogonal zero-order Bessel functions

$$\mathrm{cor}_r[\hat{\psi}](k_z, \delta r) = \sum_{i=1}^{M} E_i \cdot J_0(k_{H_i} \delta r). \qquad (12)$$

Zero-order Bessel functions are the appropriate expansion functions for isotropic measurements of a horizontal wave field (Garrett and Munk 1975; D'Asaro and Perkins 1984). The k_{H_i} are chosen so that $J_0'(k_{H_i}L) = -J_1(k_{H_i}L) = 0$, where L is the largest scale for which the correlation is known (7 km here). This ensures that the J_0 form a complete orthogonal set (Hildebrand 1976, 5.13). Given the range of scales covered by the surveys, $M = 6$ is appropriate. The fitting coefficients E_i correspond to kinetic energies KE_i for $\psi = u$ or v and potential energies PE_i for $\psi = b/\bar{N}$ ($\equiv -\bar{N}\xi$). To prevent aphysical negative coefficients, a single-value decomposition routine that constrains coefficients to be nonnegative (Menke 1989) was employed.

The fits from (12) (solid curves in Fig. 5) resemble the large-scale structure of the smoothed correlations (dashed curves) and, therefore, represent reasonable descriptions of the data. As seen in Fig. 5, and typical of other vertical wavelengths as well, the fits have values well below $\langle \mathrm{cor}_r[\hat{\psi}] \rangle$ at $\delta r = 0$ (squares). This implies that a significant fraction of the residual energy is incoherent; the incoherent energy is the difference between the average correlation at $\delta r = 0$ and the fit (12) evaluated at $\delta r = 0$. In both surveys, the averages contain over half the energy (7–12 cm^2 s^{-2}), the incoherent fractions 20%–35% (3–4 cm^2 s^{-2}) and the resolved fraction less than 10% (1 cm^2 s^{-2}) of the total.

5. Results

a. Energy versus length scale Burger numbers

The energy ratios $R_E = \mathrm{PE}/\mathrm{KE}$ are displayed in Fig. 6 as a function of normalized aspect ratio
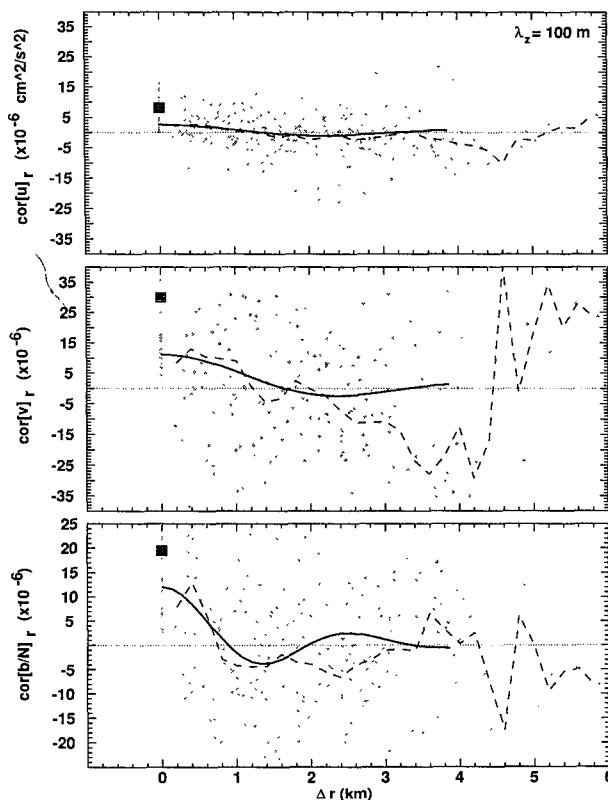

FIG. 5. The real part of the dropped lagged correlation as a function of profile-pair separation δr from survey 1 for $\lambda_z = 100$ m. Small gray dots correspond to individual pair correlations, dashed curves to radially smoothed correlations (excluding $\delta r = 0$ pairs), large solid squares at $\delta r = 0$ to the average covariance, and solid curves to least-squares fits to a sum of orthogonal zero-order Bessel functions. The similarity of the dashed and solid curves is an indication of the quality of the fit. The fit values at $\delta r = 0$ are smaller than the covariance, indicating that much of the residual variance is incoherent.

$$R_L = (Nk_H/fk_z)^2$$

for the average, resolved, and incoherent fractions. Nearest-neighbor spectral smoothing was applied in k_H and k_z space for the resolved fractions. Rossby numbers are all less than 0.2 so only the internal wave (3) and geostrophic (4) consistency relations are displayed for guidance.

For the near-seamount survey 1 (Fig. 6a), the *average* ratios (horizontal bars extending to low normalized aspect ratio R_L) are ambiguous because the aspect ratio is not known. In particular, the $\lambda_z = 400$ m ratio crosses both the internal wave and geostrophic relations, so the energy could be pure internal wave, pure geostrophic, or some mixture. Even ratios that terminate near a theoretical relation are ambiguous because R_L could be lower. Most of the average energy ratios terminate (within their error bars) between the near-inertial internal wave (dotted) or geostrophic (dashed) curves, implying near-inertial waves contributing most of the kinetic energy and geostrophic mo-
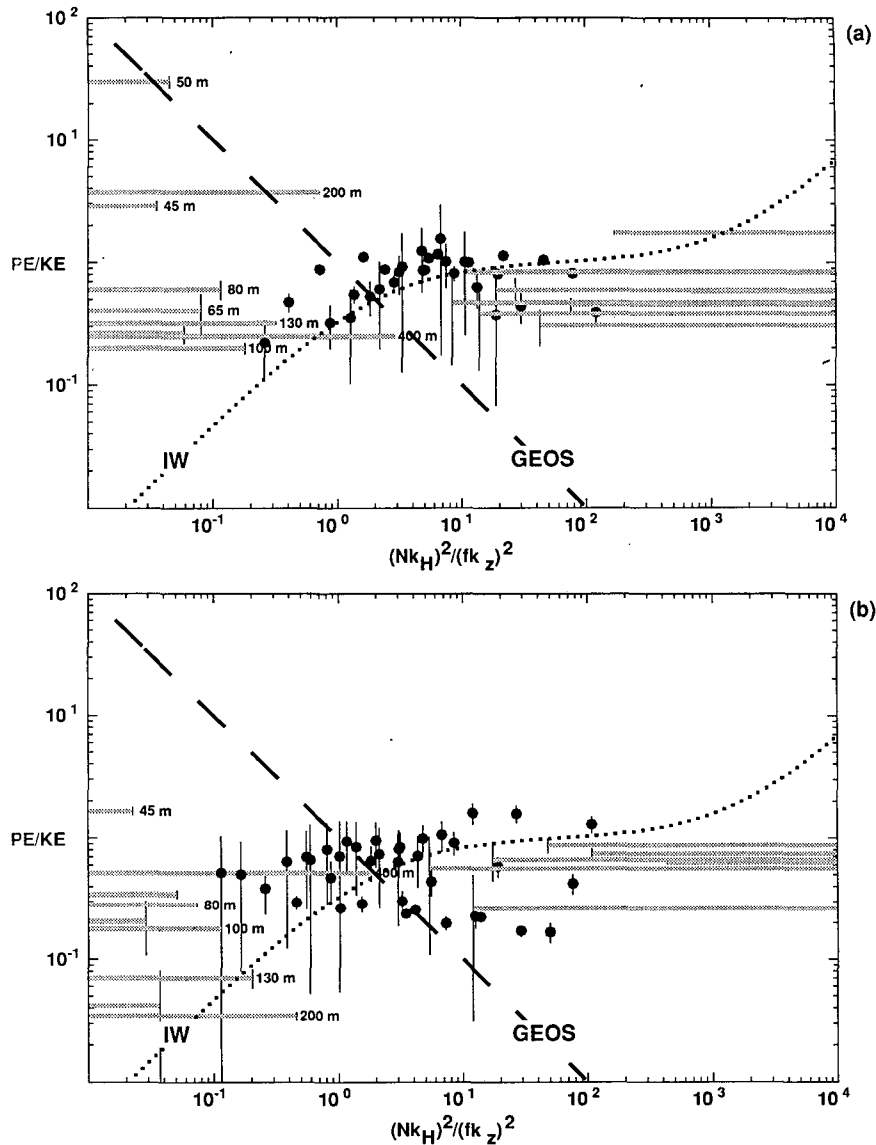
FIG. 6. The energy ratio PE/KE versus normalized aspect ratio $(Nk_H/fk_z)^2$ in (a) survey 1 and (b) survey 2 for $\lambda_z = 50$–400 m. As in Fig. 2, the thick dotted curve corresponds to linear internal waves (3) and the thick dashed curve to geostrophy (4). Horizontal bars on the left labeled by their vertical wavelength correspond to survey horizontal averages (k_H unresolved but bounded above), dots to resolved energies, and horizontal bars on the right to incoherent energies (k_H unresolved but bounded below). Smaller error bars (vertical lines) correspond to greater energy. The resolved energies in survey 1 (a) cluster around the internal wave curve. The average energy ratio for $\lambda_z = 400$ m in survey 2 (b) terminates at the intersection of the theoretical geostrophic and internal wave relations.

tions most of the potential energy. Geostrophic energy at $\lambda_z = 50$ m (Fig. 6a) is consistent with the conclusions of Kunze and Sanford (1993) based on the Ertel vorticity signature (their Fig. 11).

For $R_L > 4$, the resolved energy ratios (dots) cluster about the internal wave continuum. At lower aspect ratios (higher k_z), the energy ratios either lie between the internal wave and geostrophic curves, suggesting kinetic energy contributed by near-inertial waves and

potential energy by geostrophy, or close to their intersection.

The incoherent ratios (horizontal bars extending to high R_L) lie slightly below the internal wave continuum relation, signifying excess kinetic energy. This might be explained by the presence of small horizontal scale geostrophic motions as found by D'Asaro and Morehead (1991) under the ice in the Beaufort Sea.

For survey 2 (Fig. 6b), most of the *average* energy ratios (horizontal bars extending toward low R_L) intersect the near-inertial branch of the internal wave curve (dotted) or lie between it and the geostrophic curve (dashed). The energy ratio at $\lambda_z = 400$ m contains most of the energy in this survey (Fig. 3b) and terminates ambiguously at the intersection of the internal wave and geostrophic relations, therefore, it cannot be ascribed to geostrophy or internal waves on the basis of this consistency relation. Kunze and Sanford (1993) showed that these scales were geostrophic on the basis of their Ertel vorticity signal (Fig. 7b).

For $R_L < 2$, the *resolved* energy ratios (dots) lie between the near-inertial and geostrophic relations. At higher aspect ratios R_L (lower k_z), the ratios split, half tending to cluster near the internal wave curve and half near geostrophy. As in survey 1, the *incoherent* energy ratios lie just below the internal wave continuum relation due to excess kinetic energy.

b. Partitioning

At any instant and location, kinetic and potential energies are given by

$$KE = \frac{v \cdot v}{2} = \frac{v_{IW}^2 + 2v_{IW} \cdot v_g + v_g^2}{2}$$

$$PE = \frac{b^2}{2N^2} = \frac{b_{IW}^2 + 2b_{IW}b_g + b_g^2}{2N^2}.$$

In a temporal average, the cross terms $v_{IW} \cdot v_g$ and $b_{IW}b_g$ will vanish because of the differing intrinsic frequencies of internal waves ($f < \omega < N$) and geostrophy ($\omega = 0$). Likewise, an ensemble average of many independent realizations will have vanishing $v_{IW} \cdot v_g$ and $b_{IW}b_g$. Thus, with the observed ratio of potential-to-kinetic energy,

$$R_E = \frac{PE_g + PE_{IW}}{KE_g + KE_{IW}}, \quad (13)$$

at each normalized aspect ratio along with the known energy ratios for linear internal waves R_{IW} (3) and geostrophic motion R_g (4), it is possible to quantify the fractions of potential and kinetic energy in internal waves and geostrophy

$$\frac{KE_{IW}}{KE_{TOT}} = \frac{R_g - R_E}{R_g - R_{IW}} \qquad \frac{KE_g}{KE_{TOT}} = 1 - \frac{KE_{IW}}{KE_{TOT}} \quad (14)$$

$$\frac{PE_{IW}}{PE_{TOT}} = \frac{R_{IW}(R_E - R_g)}{R_E(R_{IW} - R_g)} \qquad \frac{PE_g}{PE_{TOT}} = 1 - \frac{PE_{IW}}{PE_{TOT}} \quad (15)$$

provided that R_E lies between R_g and R_{IW}.

This partitioning was applied to the average ($\langle \cdot \rangle$), resolved ($\sim$), and incoherent ($'$) fractions of the data. This methodology has the advantage over trying to estimate the Ertel vorticity (Kunze and Sanford 1993) that it does not require distinguishing vorticity and di-

vergence or the signs of vortex stretching and vorticity. We caution that the surveys do not contain many independent realizations at larger vertical and horizontal wavelengths. Therefore, the cross terms may not vanish in the average fraction or in the largest vertical wavelength of the resolved fraction.

Because of uncertainties in the energy and aspect ratios (Fig. 6), the estimates can be biased toward internal waves or geostrophy. In fact, using only the energy ratios, the bulk of the *average* energy cannot be assigned unambiguously to either internal waves or geostrophy. Additional constraints must be brought to bear to distinguish between the two.

The relationships between the linear Ertel vorticity perturbation, $f b_z + \zeta \bar{N}^2$, vortex stretching $f b_z$, relative vorticity ζ, and horizontal divergence ∇ (Fig. 7) provide additional restrictions on the *averages*, but because these quantities require fitting over the smaller scales, they cannot be determined for the resolved and incoherent fractions. For linear internal waves, the relative vorticity and vortex stretching cancel ($f b_z = -\zeta \bar{N}^2$) to produce zero linear Ertel vorticity anomaly ($f b_z + \zeta \bar{N}^2 \ll f b_z$). Thus, $\zeta \bar{N}^2$ and $f b_z$ must have equal variance for linear internal waves. Moreover, horizontal divergence exceeds relative vorticity for internal waves

$$(\nabla^2/\zeta^2 = \omega^2/f^2).$$

For geostrophic fluctuations, the vorticity should greatly exceed the divergence ($\nabla^2/\zeta^2 \simeq 0$), and the vortex stretching and relative vorticity are in phase with $f b_z/\zeta \bar{N}^2 = 1/R_L$ (Hoskins et al. 1985; Kunze and Sanford 1993). Thus, for example in survey 2 at $\lambda_z = 400$ m where the average energy ratio terminates ambiguously near the intersection of the internal wave and geostrophic relations (Fig. 6b), (i) the vortex stretching and relative vorticity are comparable but of the same sign so that the linear Ertel vorticity anomaly exceeds both, and (ii) the divergence is much smaller than the vorticity (Fig. 7b). Thus, we can assign the $\lambda_z = 400$ m potential and kinetic energy to geostrophy. At most other wavenumbers, there appears to be a mixture of internal wave and geostrophic contributions with geostrophy providing most of the vortex stretching (potential energy) and both internal waves (divergence) and geostrophy (vorticity in excess of divergence) contributing the kinetic energy (Fig. 7b).

Tables 1 and 2 summarize the partition of horizontal average, resolved, and incoherent energies into internal wave and geostrophic fractions for $\lambda_z = 50$–400 m. Tables 3 and 4 isolate the smaller scales ($\lambda_z = 50$–200 m). In survey 1, the *average* potential energy at $\lambda_z = 400$ and 200 m is geostrophic because $f b_z \gg \zeta \bar{N}^2$ (Fig. 7a), while the kinetic energy is ascribable to internal waves because $\nabla \gg \zeta$. At $\lambda_z = 100$ and 130 m, the vorticity and vortex-stretching are comparable and oppose each other as with internal waves while vorticity exceeds divergence like geostrophy. We interpret this as indicating a mixture of internal waves and geostro-
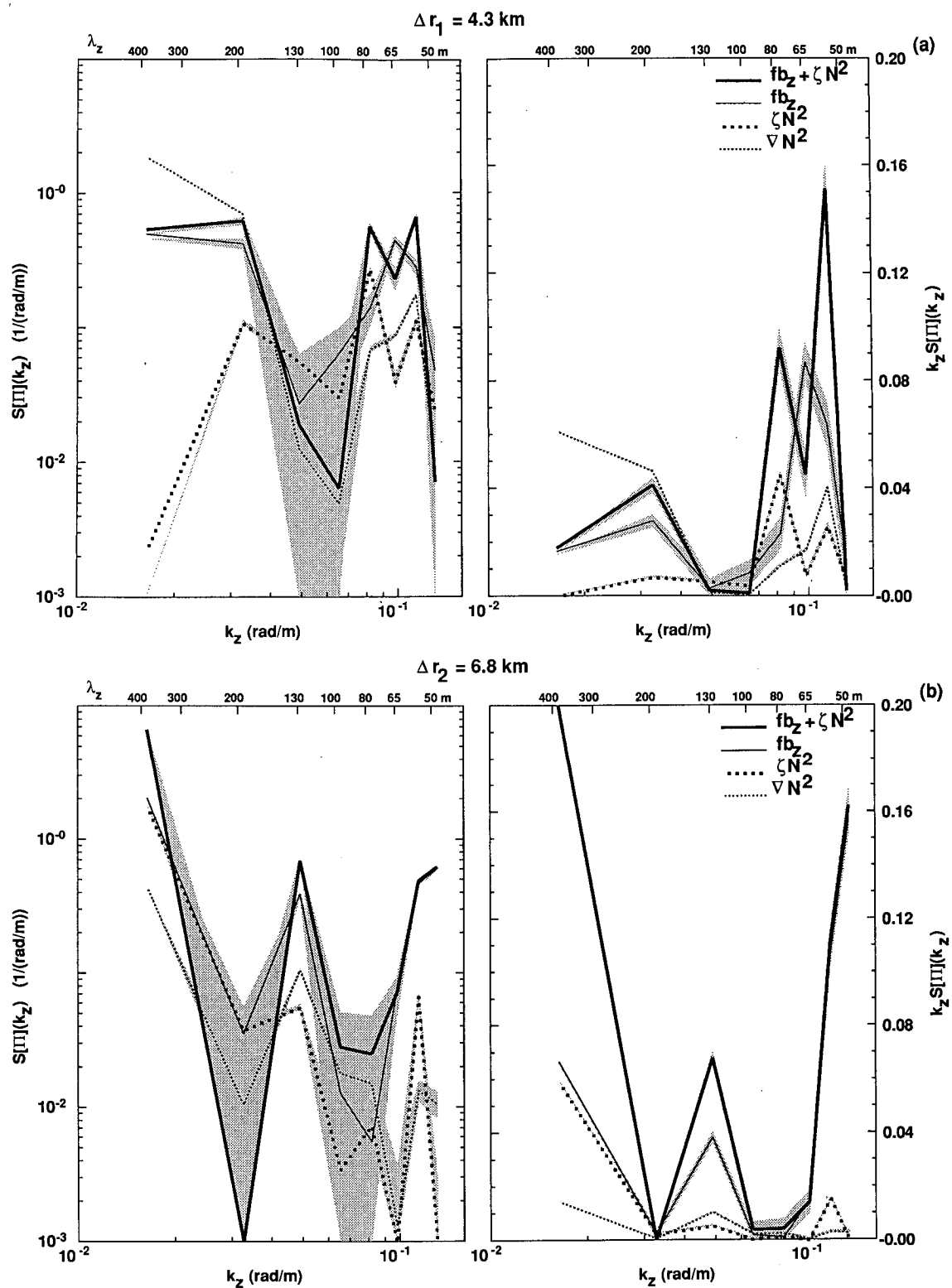
FIG. 7. Vertical wavenumber spectra of the linear Ertel vorticity perturbation, $fb_z + \zeta \bar{N}^2$, vortex-stretching fb_z, relative vorticity $\zeta \bar{N}^2$, and horizontal divergence $\nabla \bar{N}^2$ (all normalized by fN_0^2) in survey 1 (a) and survey 2 (b). The stippling represents the standard deviation, which is large for vortex stretching and otherwise comparable to the thickness of the curves.

TABLE 1. Partition of kinetic and potential energy (in cm² s⁻²) between internal waves and geostrophy for survey 1 and vertical wavelengths of 50–400 m.

	Average		Resolved		Incoherent	
	$\langle KE \rangle$	$\langle PE \rangle$	$\widetilde{KE}$	$\widetilde{PE}$	KE'	PE'
IW	**4.8**	0.3	**0.4**	**0.4**	1.0	**1.5**
Geos	0.0	**1.1**	0.1	0.1	1.2	0.0
Either	0.0	0.3	0.1	0.0	0.2	0.0
GM	2.9	0.4	1.4	0.9	0.3	0.3
Total	4.8	1.7	0.6	0.5	2.4	1.5

TABLE 3. Partition of kinetic and potential energy (in cm² s⁻¹) between internal waves and geostrophy for survey 1 and vertical wavelengths of 50–200 m.

	Average		Resolved		Incoherent	
	$\langle KE \rangle$	$\langle PE \rangle$	$\widetilde{KE}$	$\widetilde{PE}$	KE'	PE'
IW	**0.42**	0.00	**0.20**	**0.18**	0.35	**0.54**
Geos	0.01	**0.06**	0.07	0.08	0.22	0.00
Either	0.00	0.04	0.08	0.04	0.22	0.05
GM	1.08	0.08	0.93	0.46	0.21	0.20
Total	0.43	0.10	0.35	0.30	0.79	0.59

phy. At $\lambda_z = 50$ m, PE/KE crosses the geostrophic curve (Fig. 6a) and $f b_z \gg \zeta \bar{N}^2$ (Fig. 7a), consistent with geostrophy. At $\lambda_z = 80$, 65, and 45 m, average kinetic energy is attributable to internal waves and average potential energy to geostrophy (Figs. 6a and 7a).

The *resolved* and *incoherent* potential energies and resolved kinetic energy are attributable to internal waves while the *incoherent* kinetic energies exceed internal wave predictions by a factor of two (Tables 1 and 3). This is commensurate with the D'Asaro and Morehead (1991) finding that geostrophic (or vortical) kinetic energies dominated on small horizontal scales in the Beaufort Sea.

For survey 2 (Tables 2 and 4), the *average* energies $\langle KE \rangle$ and $\langle PE \rangle$ at $\lambda_z = 400$ m can be attributed to geostrophy because the linear Ertel vorticity anomaly $f b_z + \zeta \bar{N}^2$ exceeds the vortex stretching $f b_z$ and relative vorticity $\zeta \bar{N}^2$ terms, and vorticity ζ exceeds divergence ∇ (Fig. 7b). At smaller vertical wavelengths, internal waves contribute most of the kinetic energy, and geostrophy most of the potential energy since $f b_z \gg \zeta \bar{N}^2$ but $\nabla \geq \zeta$.

Most of the *resolved* energy is geostrophic though there is some internal wave energy at smaller vertical wavelengths. A significant portion of the resolved energy cannot be assigned to either internal waves or geostrophy because it lies outside the domain bound by the theoretical curves (Fig. 6b). This may be because these measurements do not represent true statistical averages as discussed in conjunction with (13). If both geostrophic and internal fluctuations are present and of similar magnitude, the cross terms may interfere. As in survey 1, the *incoherent* potential energy is entirely attributable to internal waves but there is excess kinetic energy.

In summary, both internal waves and geostrophy contribute to fluctuations on $\lambda_H \sim 0.5$–20 km and $\lambda_z = 50$–400 m beside Ampere Bank in the eastern North Atlantic.

6. Conclusions

Using two velocity and temperature profile surveys collected beside Ampere Seamount, the dependence of the ratio of available potential to horizontal kinetic energy $R_E = PE/KE$ on the normalized aspect ratio $R_L = (N k_H / f k_z)^2$ has been compared with the theoretical relations for linear internal waves (3) and geostrophy (4) in Fig. 6. Neglect of nonlinearity is justified because Rossby numbers are less than 0.2. Utilizing

TABLE 2. Partition of kinetic and potential energy (in cm² s⁻²) between internal waves and geostrophy for survey 2 and vertical wavelengths of 50–400 m. Most of the kinetic and potential energy is in the average at $\lambda_z = 400$ m. It could not be discerned whether it is internal waves or geostrophy using the analysis technique described in the text (Fig. 6b). However, examination of the relative vorticity, horizontal divergence, vortex stretching, and Ertel vorticity reveals that it is geostrophic (Kunze and Sanford 1993).

	Average		Resolved		Incoherent	
	$\langle KE \rangle$	$\langle PE \rangle$	$\widetilde{KE}$	$\widetilde{PE}$	KE'	PE'
IW	1.1	0.0	0.1	0.1	1.0	**1.3**
Geos	**7.2**	**3.9**	**0.5**	0.1	0.9	0.0
Either	0.0	0.0	0.1	0.1	0.2	0.0
Neither	0.0	0.0	0.2	0.1	0.0	0.0
GM	2.9	0.4	1.4	0.9	0.3	0.3
Total	8.3	3.9	0.9	0.3	2.1	1.3

TABLE 4. Partition of kinetic and potential energy (in cm² s⁻²) between internal waves and geostrophy for survey 2 and vertical wavelengths of 50–200 m.

	Average		Resolved		Incoherent	
	$\langle KE \rangle$	$\langle PE \rangle$	$\widetilde{KE}$	$\widetilde{PE}$	KE'	PE'
IW	**1.06**	0.00	0.16	0.04	0.20	**0.24**
Geos	0.00	**0.09**	0.09	0.01	0.11	0.00
Either	0.00	0.04	0.10	0.06	0.20	0.06
Neither	0.00	0.00	0.23	0.08	0.00	0.00
GM	1.08	0.08	0.93	0.46	0.21	0.20
Total	1.06	0.13	0.58	0.19	0.51	0.30

the theoretical relations, the kinetic and potential energies were partitioned into internal wave and geostrophic fractions for horizontal averages ($\lambda_H > 7$ km), resolved horizontal wavelengths ($\lambda_H = 1$–7 km), and horizontally incoherent parts ($\lambda_H < 1$ km) (Tables 1–4). Assignment of the *average* energy was ambiguous because the horizontal wavenumber (length scale Burger number) can only be bounded above (Fig. 6) so additional information was brought to bear by examining the vortex stretching, relative vorticity, and horizontal divergence on these scales (Fig. 7).

In survey 1, geostrophy contributes most of the average potential energy and internal waves most of the average kinetic energy (Tables 1 and 3). Geostrophy dominates the averages in survey 2 at $\lambda_z = 400$ m (Table 2), while internal waves dominate at smaller vertical wavelengths (Table 4). The energy in the resolved fractions in both surveys is mostly from internal waves except for a large contribution from geostrophy at $\lambda_z = 400$ m in survey 2. A significant fraction of the survey 2 resolved energy could not be accounted for, probably because the surveys do not provide an average of many independent realizations for larger vertical wavelengths. The *incoherent* potential energy is entirely attributable to internal waves. There is twice as much incoherent kinetic energy as the internal wave relation (3) predicts. This can be ascribed to geostrophic motion as in D'Asaro and Morehead's (1991) surveys in the Beaufort Sea. At 0.2 cm^2 s^{-2}, their incoherent kinetic energy is comparable to the geostrophic component at $\lambda_z = 50$–200 m found here (Tables 3 and 4) and three times larger than high-frequency internal wave energy in the weak internal wave environment under the ice. This part of the Arctic Ocean is known to contain many small eddies (Manley and Hunkins 1985; D'Asaro 1988a), which D'Asaro (1988b) argues are generated by frictional torques in Barrow Canyon.

Both internal waves and geostrophy appear to contribute on all vertical and horizontal scales beside Ampere Bank. This conclusion is consistent with the Ertel vorticity analysis of this same dataset (Kunze and Sanford 1993). Kunze and Sanford (1993) argue that irreversible processes on the seamount's flanks induce submesoscale Ertel vorticity anomalies (geostrophic fluctuations), which are not necessarily characteristic of the ocean interior away from topography.

Kunze et al. (1990) applied similar relations to 1–5-m shear and strain in a midlatitude pycnocline. They had no measurements of the horizontal structure and therefore had to rely on the finescale aspect ratio being "typical," $(N\lambda_z/f\lambda_H)^2 = 0.001$–0.1 (Marmorino et al. 1987; Gregg et al. 1986; Itsweire et al. 1989), to argue that the finescale was dominated by near-inertial waves. However, the semi-Lagrangian spectra of Sherman and Pinkel (1991) and Anderson and Pinkel (1993) support their contention that most shear variance at high wavenumber is Doppler-smeared near-

inertial motions rather than Ertel vorticity–carrying fluctuations.

Determining the relative contributions of internal waves and geostrophy on the scales traditionally ascribed to internal waves deserves continued research. Horizontal mixing due to vertical shear dispersion is particularly sensitive to the intrinsic frequency of motion. Young et al. (1982) find horizontal diffusivities due to shear dispersion of

$$K_H = \frac{1}{4} \frac{K_z V_z^2}{\omega^2 + K_z^2 k_z^4},$$

which yields $K_H \approx 0.01$ m^2 s^{-1} for $K_z = 10^{-5}$ m^2 s^{-1} and typical internal wave parameters ($\omega = f = 10^{-4}$ s^{-1}, $V_z = N = 5 \times 10^{-3}$ s^{-1}, $k_z = 2\pi/10$ m^{-1}) while, because of the inverse dependence on frequency, $K_H \geq 1$ m^2 s^{-1} as observed (Ledwell et al. 1993) for subinertial shear of $0.1 N$ and frequency $\omega \leq 0.01 f$. Thus, Ertel vorticity–carrying shear is much more efficient at shear dispersion than internal waves, and even a small contribution from Ertel vorticity–carrying dynamics could substantially enhance horizontal mixing. Unaddressed here or in Kunze and Sanford (1993) are the relative contributions of internal waves and Ertel vorticity–carrying fluctuations on wavelengths $\lambda_z < 50$ m, which contribute the most vertical shear in the ocean.

Expendable technology proved valuable in this study because of its small velocity noise (~ 0.4 cm s^{-1}) and its facility to be deployed rapidly from a ship under way. But it is not without limitations. At present, it is restricted in its range of resolved horizontal and vertical scales by relatively large temperature uncertainties ($\sim 0.06°$C) and by temporal aliasing of horizontal structure during the course of a survey. Moorings would overcome the temporal aliasing problem, but at least ten would be needed to adequately distinguish relative vorticity from horizontal divergence (Lien and Müller 1992b) on the submesoscale, and dense vertical sampling would be required to account for the effects of internal wave isopycnal displacements.

REFERENCES

Anderson, S. P., and R. Pinkel, 1993: Observations of semi-Lan-grangian finestructure. *J. Phys. Oceanogr.,* submitted.

D'Asaro, E. A., 1988a: Observations of small eddies in the Beaufort Sea. *J. Geophys. Res.,* **93,** 6669–6684.

D'Asaro, E. A., 1988b: Generation of submesoscale vortices: A new mechanism. *J. Geophys. Res., 94*, 6685–6693.

——, and H. Perkins, 1984: A near-inertial internal wave spectrum for the Sargasso Sea in late summer. *J. Phys. Oceanogr., 14*, 489–505.

——, and M. D. Morehead, 1991: Internal waves and velocity finestructure in the Arctic Ocean. *J. Geophys. Res., 96*, 12 725–12 738.

Ertel, H., 1942: Ein neuer hydrodynamischer Wirbelsatz. *Meteorol. Z., 83*, 2989–3009.

Fofonoff, N. P., 1969: Spectral characteristics of internal waves in the ocean. *Deep-Sea Res., 16* (Suppl.), 58–71.

Garrett, C. J. R., and W. Munk, 1975: Space-time scales of internal waves: A progress report. *J. Geophys. Res., 80*, 291–297.

——, and W. Munk, 1979: Internal waves in the ocean. *Annu. Rev. Fluid Mech., 11*, 339–369.

Gregg, M. C., E. A. D'Asaro, T. J. Shay, and N. Larson, 1986: Observations of persistent mixing and near-inertial internal waves. *J. Phys. Oceanogr., 16*, 856–885.

Haynes, P. H., and M. E. McIntyre, 1987: On the evolution of vorticity and potential vorticity in the presence of diabatic heating and frictional or other forces. *J. Atmos. Sci., 44*, 828–841.

Herring, J. A., and O. Metais, 1989: Numerical experiments in forced stably-stratified turbulence. *J. Fluid Mech., 202*, 97–115.

Hildebrand, F. B., 1976: *Advanced Calculus for Applications,* 2d ed. Prentice-Hall, 733 pp.

Holloway, G., 1983: A conjecture relating oceanic internal waves and small-scale processes. *Atmos.-Ocean, 31*, 107–122.

Hoskins, B. J., M. E. McIntyre, and R. W. Robertson, 1985: On the use and significance of isentropic potential vorticity maps. *J. Roy. Meteor. Soc., 111*, 877–946.

Itsweire, E. C., T. R. Osborn, and T. P. Stanton, 1989: Horizontal distribution and characteristics of shear layers in the seasonal thermocline. *J. Phys. Oceanogr., 19*, 301–320.

Kennelly, M. A., M. D. Prater, J. H. Dunlap, E. Kunze, and T. B. Sanford, 1989: XCP data from the Gulf of Cadiz Expedition: R/V *Oceanus* Cruise 202. Tech. Rep. 8925, Appl. Phys. Lab., University of Washington, Seattle, WA, 206 pp.

Kunze, E., and T. B. Sanford, 1993: Submesoscale dynamics near a seamount. Part I: Measurements of Ertel vorticity. *J. Phys. Oceanogr., 23*, 2567–2588.

——, M. G. Briscoe, and A. J. Williams III, 1990: Interpreting shear and strain finestructure from a neutrally-buoyant float. *J. Geophys. Res., 95*, 18 111–18 125.

Ledwell, J. R., A. J. Watson, and C. S. Law, 1993: Evidence of slow mixing across the pycnocline from an open-ocean tracer-release experiment. *Nature, 364*, 701–703.

Lelong, M.-P., and J. J. Riley, 1992: Internal wave–vortical mode interactions in strongly-stratified flows. *J. Fluid Mech., 232*, 1–19.

Lien, R.-C., and P. Müller, 1992a: Consistency relations for gravity and vortical modes in the ocean. *Deep-Sea Res., 39*, 1595–1612.

——, and ——, 1992b: Normal-mode decomposition of smallscale oceanic motions. *J. Phys. Oceanogr., 22*, 1583–1595.

Lilly, D. K., 1983: Stratified turbulence and the mesoscale variability of the atmosphere. *J. Atmos. Sci., 40*, 749–760.

Manley, T. O., and K. Hunkins, 1985: Mesoscale eddies of the Arctic Ocean. *J. Geophys. Res., 90*, 4911–4930.

Marmorino, G. O., L. J. Rosenblum, and C. L. Trump, 1987: Finescale temperature variability: The influence of near-inertial waves. *J. Geophys. Res., 92*, 13 049–13 062.

Menke, W., 1989: *Geophysical Data Analysis: Discrete Inverse Theory.* Academic Press, 289 pp.

Müller, P., 1984: Smallscale vortical motions. Internal gravity waves and small-scale turbulence. *Proc. 'Aha Huliko'a Hawaiian Winter Workshop,* P. Müller and R. Pujalet, Eds., Hawaiian Inst. Geophys., 249–262.

——, and G. Siedler, 1976: Consistency relations for internal waves. *Deep-Sea Res., 23*, 613–628.

——, D. J. Olbers, and J. Willebrand, 1978: The IWEX spectrum. *J. Geophys. Res., 83*, 479–500.

——, R.-C. Lien, and R. Williams, 1988: Estimates of potential vorticity at small scales in the ocean. *J. Phys. Oceanogr., 18*, 401–416.

Pedlosky, J., 1979: *Geophysical Fluid Dynamics.* Springer-Verlag, 624 pp.

Riley, J. J., R. W. Metcalfe, and M. A. Weissman, 1981: Direct numerical simulations of homogeneous turbulence in density-stratified fluids. *Nonlinear Properties of Internal Waves,* B. J. West, Ed., Amer. Inst. Phys., 76, 79–112.

Sanford, T. B., R. G. Drever, J. H. Dunlap, and E. A. D'Asaro, 1982: Design, operation and performance of an expendable temperature and velocity profiler (XTVP). Tech. Rep. 8110, Appl. Phys. Lab., University of Washington, 83 pp.

Sherman, J. T., and R. Pinkel, 1991: Estimates of the vertical wave-number-frequency spectra of vertical shear and strain. *J. Phys. Oceanogr., 21*, 292–303.

Young, W. R., P. B. Rhines, and C. J. R. Garrett, 1982: Shear-flow dispersion, internal waves and horizontal mixing in the ocean. *J. Phys. Oceanogr., 12*, 515–527.